

# Dynamic Analysis of Spin Satellites Through the Quadratic Phase Estimation in Multiple-Station Radar Images

Yejian Zhou<sup>ID</sup>, Lei Zhang<sup>ID</sup>, Shaopeng Wei, and Yunhe Cao

**Abstract**—Dynamic analysis of in-orbit satellites is of interest for space situation applications. Some exploratory methods have been presented to analyze the state of attitude-stabilized satellites in the complex space situation, but effectively estimating the dynamic parameters of spinning satellites remains a significant and interesting challenge nowadays. With decoupling target spin estimation from its trajectory motion, this paper proposes a novel dynamic estimation approach by using multiple-station inverse synthetic aperture radar (ISAR) images. In brief, quadratic phase characteristic, which is usually regarded as a negative factor for ISAR imagery in conventional algorithms, is now directly exploited to build an explicit expression of the relative motion between the spin in-orbit satellite and radar. Then, based on the developed image refocusing algorithm, these phase coefficients are extracted from the multiple-station images and substituted into the optimization of target dynamic estimation. In the end, target dynamic parameters, including its instantaneous attitude vector and spin speed, are estimated through particle swarm optimization. Experiment results illustrate the feasibility of the proposed algorithm. To some degree, this work also reflects the advantages of multiple-station ISAR system in some space applications.

**Index Terms**—Inverse synthetic aperture radar (ISAR) imaging, target dynamic estimation, radar image refocusing, multiple-station image interpretation.

## I. INTRODUCTION

**I**N PAST decades, as more and more satellites operated for various purposes have been launched into space, the satellite dynamic monitoring has become a hot issue in space situation awareness (SSA) research [1]–[7]. Dynamic estimation proves essential for avoiding collisions, especially in the case of uncontrolled satellites in orbit. Due to aerodynamics reasons [8]–[10],

Manuscript received January 7, 2020; revised April 8, 2020; accepted May 11, 2020. Date of publication May 15, 2020; date of current version June 15, 2020. This work was supported in part by the National Natural Sciences Foundation of China under Grants 61771372 and 61771367, and in part by Shenzhen Science and Technology Program. The associate editor coordinating the review of this manuscript and approving it for publication was Francesco Soldovieri. (*Corresponding author: Lei Zhang.*)

Yejian Zhou, Shaopeng Wei, and Yunhe Cao are with the National Lab of Radar Signal Processing and the Collaborative Innovation Center of Information Sensing and Understanding, Xidian University, Xi'an 710071, China (e-mail: zhouchujian25@163.com; spw\_xd@163.com; caoyunhe@mail.xidian.edu.cn).

Lei Zhang is with the School of Electronics and Communication Engineering, Sun Yat-Sen University (Shenzhen campus), Shenzhen 518100, China (e-mail: zhanglei57@mail.sysu.edu.cn).

Digital Object Identifier 10.1109/TCI.2020.2995052

some of these satellites could spin in space, leading to the dimension increase of their dynamic estimation. Therefore, compared with controlled in-orbit satellites, the dynamic state analysis for these satellites is more difficult in practical applications.

Reviewing the relevant literature, most conventional ego-motion estimation methods fail to determine the state parameters of uncontrolled spin satellites when the satellites stop reporting their states or conveying observation data to the ground [6], [7]. Several exploratory studies have been proposed utilizing exterior measurement achieved through advanced space-borne or ground-based remote sensing equipment, like inverse synthetic aperture radar (ISAR)[11]–[18], in order to obtain the state parameters. Organized by German Fraunhofer FHR laboratory, the Tracking and Imaging Radar (TIRA) was adopted to for the continuous tracking of Envisat from 2011 to 2017 [19], [20]. According to the labeled simulation images, an engineering software can be utilized to map the acquired ISAR imagery in order to determine the target instantaneous attitude [20]. In another sort of method, the ISAR target geometry has been taken into the consideration during interpreting the high-resolution ISAR image sequence [21]–[23] to obtain the instantaneous attitude of satellite. Based on different features change among the observation sequence, the target absolute attitude will be estimated when these features are exactly extracted and associated. However, it is still a challenge to achieve precise dynamic estimation for spin satellites as the change of the observation imaging planes for ISAR imaging is often coupled with the satellite spin motion. As a result, technological difficulties in areas such as image scaling and sequential feature association limit the feasibility of these existing methods. Briefly, dynamic estimation for spin satellite centers on effectively determining the relationship between the target motion parameters and its features included in radar echo.

Recently, a noteworthy work [24] was presented to exploit the phase characteristic of ISAR imagery to estimate target absolute attitude in the current coherent processing interval (CPI) instead of the long-term sequential processing. The main idea of this work is that the high order phase terms in radar images, usually regarded as the unexpected information and compensated during the imaging processing, are extracted and explicitly embedded in the target attitude estimation. Although this work aims at stable-attitude satellites, it might be a potential way to estimate the dynamic parameters of spin satellites, motivating the work in this paper. Following Ref. [24], the intrinsic

connection between the target dynamic parameters and phase characteristics of acquired ISAR imagery is concluded with an explicit expression. Furthermore, multiple-station ISAR system is adopted to solve the dimension increasing of the parameter estimation. The superiority of multiple-station ISAR system has been demonstrated in various applications[25]–[31], and some subspace-based methods are potentially applicable in improving the resolution and focusing performance of these images [47], [48]. In this work, target multiple-angle motion feature resulting from the image defocusing phenomenon is extracted from synchronized multiple-station images. Then, it is used to draw target instantaneous dynamic parameters in each imaging CPI, without building a complex sequential model of target motion in single-station observation.

A brief flow of the proposed method is given below. First, the ISAR imaging geometry model of the spin satellite in orbit is built and the relative motion between target and radar is split into two parts, the target trajectory and spin motion. The multiple-station radar line of sight (LOS) parameters, loaded from radar tracking systems, are substituted into the derived expression which explains the relationship between target instantaneous dynamic parameters and the phase characteristics of defocused ISAR images. After that, the image defocusing coefficients of each image are extracted by the proposed image auto-focusing technology based on the image entropy minimization [32]–[39]. At last, the target dynamic parameters including instantaneous attitude and spin speed are estimated in the difference minimization of multiple-station attitude vectors solved by the particle swarm optimization (PSO) algorithm [40]–[42].

Compared with the existing methods, the proposed algorithm has some innovations.

- 1) Different from most existing works, high-order phase terms in radar image are no longer regarded as the unexpected error which damages the image quality. On the contrary, they are directly exploited to extract the target dynamic information from the observation image. As the high-order phase terms essentially reflect the relative motion between target and radar, the phase characteristics in each radar image can be directly used to interpret target dynamic information. In this way, the proposed algorithm avoids the complex feature association which limits the estimation performances of the existing sequential-based methods in a long-term radar image sequence [22], [23].
- 2) To the best of our knowledge, it is the first time that the phase characteristics of multiple-station ISAR images have been adopted in the dynamic estimation of spin in-orbit satellite. The multiple-station cooperation strategy makes up the angular limitation of the single-station observation greatly. In this paper, the phase characteristics are adopted to convert the target dynamic estimation from the sequential motion analysis to the instantaneous state estimation, addressing the dimension increasing problem in some degree. With the development of radar remote sensing technology, multiple-station information fusion will be extended to various space applications. We believe that the usage of multiple-station ISAR phase characteristics in this work provides a new viewpoint of interpreting

this kind of radar images and also has a potential capacity for multiple-band radar applications.

The remainder of the paper is organized as follows. Section II investigates the ISAR imaging geometry of the in-orbit satellite and mathematically state the relationship between the target dynamic and its image phase characteristics. Section III introduces how to use ISAR image refocusing algorithm to estimate the phase coefficient while Section IV illustrates how to use multiple-station phase coefficients to estimate target dynamic parameters. In Section V, the experiments demonstrate the feasibility of the proposed algorithm in practical applications, and some crucial conclusions are drawn in Section VI.

## II. THE SIGNAL MODEL

Unlike optical imagery, radar images include information about targets motion relative to radar sensor as the most imaging algorithms are based on the Doppler principle. By analyzing the echo signal of in-orbit spin satellite, an explicit expression is derived to bridge its dynamic parameters and ISAR image feature in this section. Based on multiple-station ISAR imaging devices, the image phase characteristics of the plane component mounted on the target is applied to interpret its dynamic parameters. Detailed derivations are below.

Since the range compression and cell migration correction have been well performed in the range-Doppler (RD) imaging algorithm, the target response signal can be written as Eq. (1) [43].

$$S(\tau, t_m) = \sum_{p=1}^P A_p \text{sinc}[\gamma T_w(\tau - \tau_p)] \times \text{rect}\left[\frac{t_m}{T_m}\right] \times \exp\left[-\frac{j4\pi R_p(t_m)}{\lambda}\right] \quad (1)$$

where index  $p$  is the serial number of scattering points,  $\text{sinc}(u) = \frac{\sin(\pi u)}{\pi u}$  is the Sinc function,  $\text{rect}(\bullet)$  refers to the rectangle window function,  $A_p$  is the signal amplitude,  $t_m$  denotes the slow-time relative to the sampling in the azimuth direction,  $\tau$  denotes the fast-time relative to the sampling in the range direction,  $\tau_p$  denotes the time-delay of the scattering point in current pulse,  $T_w$  and  $T_m$  represent the pulse duration width and the pulse repetition time respectively,  $\gamma$  is the chirp rate,  $\lambda$  represents the signal wavelength, and  $R_p(t_m)$  refers to the slant-range of the scattering center.

Assuming that the target translation is compensated well, the slant-range history of the scattering center can be understood as the inner product of itspace position and the radar LOS vector  $\vec{k}$  in the target Cartesian coordinates [44]. The expression is given as Eq. (2).

$$R_p(t_m) = \vec{p} \cdot \vec{k} = z \sin \theta(t_m) + y \cos \theta(t_m) \cos \phi(t_m) + x \cos \theta(t_m) \sin \phi(t_m) \quad (2)$$

where the scattering center position is defined as  $\vec{p} = (x, y, z)^T$ , the elevation angle  $\theta(t_m)$  is the intersection angle between the instantaneous radar LOS vector and the  $XOY$  plane, and the azimuth angle  $\phi(t_m)$  is the intersection angle between the

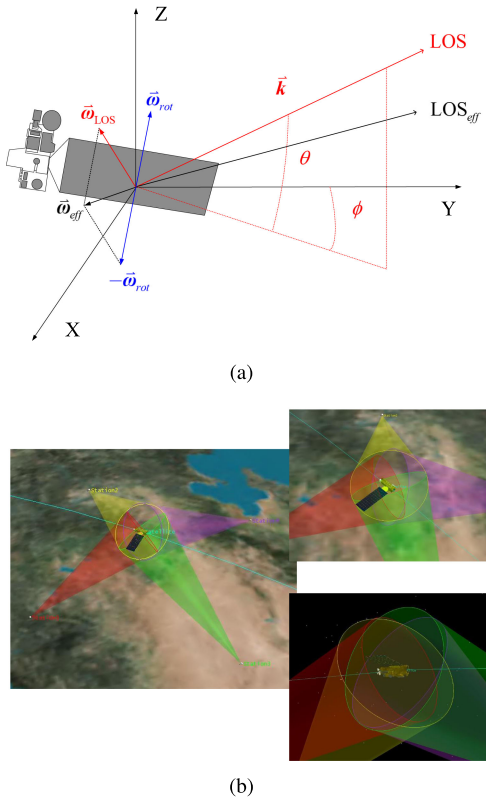


Fig. 1. The observation geometry and motion model of the spin satellite. (a) Target spin model in the target Cartesian coordinate system. (b) The observation geometry in Satellite Tool Kit software.

$Y$  axis and the projection of the instantaneous radar LOS vector in the  $XOY$  plane, as shown in Fig. 1(a).

In order to describe the relative motion between the satellite and radar in a brief way, the target position is assumed to be static during the current CPI while the LOS angle function is developed with two groups of parameters, the target trajectory parameters and spin parameters, as Eqs. (3)-(4).

$$\begin{aligned} \theta(t_m; \alpha_{\text{Tra}}, \Delta\alpha_{\text{Tra}}, \alpha_{\text{Rot}}, \Delta\alpha_{\text{Rot}}) \\ = \theta_0 + (\alpha_{\text{Tra}} + \alpha_{\text{Rot}}) t_m + (\Delta\alpha_{\text{Tra}} + \Delta\alpha_{\text{Rot}}) t_m^2 \end{aligned}$$

$$R_0(x, y, z) = z \sin \theta_0 + y \cos \theta_0 \cos \phi_0 + x \cos \theta_0 \sin \phi_0 \quad (7)$$

$$R_1(x, y, z) = z \cos \theta_0 \cdot \alpha - y [\cos \theta_0 \sin \phi_0 \cdot \beta + \sin \theta_0 \cos \phi_0 \cdot \alpha] + x [\cos \theta_0 \cos \phi_0 \cdot \beta - \sin \theta_0 \sin \phi_0 \cdot \alpha] \quad (8)$$

$$\begin{aligned} R_2(x, y, z) = z \cos \theta_0 \cdot \Delta\alpha - y [\cos \theta_0 \sin \phi_0 \cdot \Delta\beta + \sin \theta_0 \cos \phi_0 \cdot \Delta\alpha] \\ + x [\cos \theta_0 \cos \phi_0 \cdot \Delta\beta - \sin \theta_0 \sin \phi_0 \cdot \Delta\alpha] + y [\sin \theta_0 \sin \phi_0 \cdot \alpha\beta] - x [\sin \theta_0 \cos \phi_0 \cdot \alpha\beta] \end{aligned} \quad (9)$$

$$\mathbf{R} = \begin{bmatrix} R_0(x, y, z) \\ R_1(x, y, z) \\ R_2(x, y, z) \end{bmatrix} = \mathbf{T} \bullet \vec{\mathbf{p}} \quad (10)$$

$$\mathbf{T} = \begin{bmatrix} \cos \theta_0 \sin \phi_0 & \cos \theta_0 \cos \phi_0 \cdot \beta - \sin \theta_0 \sin \phi_0 \cdot \alpha & \cos \theta_0 \cos \phi_0 \cdot \Delta\beta - \sin \theta_0 \sin \phi_0 \cdot \Delta\alpha - 2 \sin \theta_0 \cos \phi_0 \cdot \alpha\beta \\ \cos \theta_0 \cos \phi_0 & -\cos \theta_0 \sin \phi_0 \cdot \beta - \sin \theta_0 \cos \phi_0 \cdot \alpha - \cos \theta_0 \sin \phi_0 \cdot \Delta\beta - \sin \theta_0 \cos \phi_0 \cdot \Delta\alpha + 2 \sin \theta_0 \sin \phi_0 \cdot \alpha\beta & \cos \theta_0 \cdot \Delta\alpha \\ \sin \theta_0 & \cos \theta_0 \cdot \alpha & \end{bmatrix}^T \quad (11)$$

$$= \theta_0 + \alpha t_m + \Delta\alpha t_m^2 \quad (3)$$

$$\begin{aligned} \phi(t_m; \beta_{\text{Tra}}, \Delta\beta_{\text{Tra}}, \beta_{\text{Rot}}, \Delta\beta_{\text{Rot}}) \\ = \phi_0 + (\beta_{\text{Tra}} + \beta_{\text{Rot}}) t_m + (\Delta\beta_{\text{Tra}} + \Delta\beta_{\text{Rot}}) t_m^2 \\ = \phi_0 + \beta t_m + \Delta\beta t_m^2 \end{aligned} \quad (4)$$

where the subscript *Tra* and *Rot* identify the relative motion caused by the target trajectory and spin motion respectively. In practice, trajectory parameters ( $\alpha_{\text{Tra}}, \Delta\alpha_{\text{Tra}}, \beta_{\text{Tra}}, \Delta\beta_{\text{Tra}}$ ) are loaded from the tracking device in the ground ISAR system, while the target spin parameters ( $\alpha_{\text{Rot}}, \Delta\alpha_{\text{Rot}}, \beta_{\text{Rot}}, \Delta\beta_{\text{Rot}}$ ) are unknown and will be estimated through the phase analysis of the multi-station ISAR imagery in this section.

Substituting Eq. (5) into Eq. (2), the slant-range history is re-written as (6) at each ground-based observation station.

$$\begin{cases} \sin(\theta + \alpha t) \approx \sin \theta + \cos \theta \cdot \alpha t \\ \cos(\theta + \alpha t) \approx \cos \theta - \sin \theta \cdot \alpha t \end{cases} \quad (5)$$

$$R_p(t_m) = R_0(x, y, z) + R_1(x, y, z)t_m + R_2(x, y, z)t_m^2 \quad (6)$$

where the constant term, the first order term and the quadratic term in the scatterer slant-range are given as Eqs. (7)–(9), shown at the bottom of this page.

In order to relate its phase characteristic to target dynamic parameters, Eqs.(7)–(8) are represented in vectors as Eqs.(10)–(11), shown at the bottom of this page.

For a two-dimensional (2D) plane  $\Omega$ , scattering points distribution can be expressed as

$$\vec{\mathbf{v}}_T \cdot \vec{\mathbf{p}} = \kappa, \vec{\mathbf{p}}(x, y, z) \in \Omega \quad (12)$$

where  $\vec{\mathbf{v}}_T$  is the normal vector of the plane component, and  $\kappa$  is the distance between the origin and the plane.

Besides, the spatial-variant phase error can be modeled as the linear expression of the target range and Doppler coordinate in the RD image [24], [38], [39].

$$R_2(x, y, z) = e_r R_0(x, y, z) + e_a R_1(x, y, z) \quad (13)$$

Then, substitute Eq. (10) into Eq. (13), it can be written as following

$$[e_r, e_a, -1]_{1 \times 3} \cdot \mathbf{T} \cdot \vec{\mathbf{p}} = 0 \quad (14)$$

Compared with Eq. (12), an explicit expression of target attitude parameters, i.e. the normal vector of a plane component, is derived from Eq. (14) as shown in Eq. (15).

$$\vec{\mathbf{v}}_T = [e_r, e_a, -1]_{1 \times 3} \cdot \mathbf{T}(\alpha_{Rot}, \Delta\alpha_{Rot}, \beta_{Rot}, \Delta\beta_{Rot}) \quad (15)$$

That is to say that we can obtain a quaternion equation as Eq. (15) in every ISAR image, and the normal vector  $\vec{\mathbf{v}}_T$  should be invariant at different ISAR observation angles, as shown in Fig. 1(b). Therefore, in order to determine these quaternary parameters, the four-station joint observation needs to be built and the optimization function is following:

$$\begin{aligned} & \min_{\mathbf{T}(\alpha_{Rot}, \Delta\alpha_{Rot}, \beta_{Rot}, \Delta\beta_{Rot})} \\ & \sum_{i=1}^3 \sum_{j=i+1}^4 \left| \vec{\mathbf{v}}_T(e_{r,i}, e_{a,i}) \bullet \vec{\mathbf{v}}_T(e_{r,j}, e_{a,j}) \right| \end{aligned} \quad (16)$$

Here, solving defocusing coefficients  $(e_r, e_a)$  in each RD imagery becomes the key to the dynamic estimation of spin satellites.

### III. ISAR IMAGE REFOCUSING

In this section, as in the previous one, the image refocusing algorithm is used to estimate the defocusing coefficients  $e_r$  and  $e_a$  in the ISAR imagery, with the aim of improving the radar image quality by compensating the quadratic or higher order phase error in ISAR imaging processing. In order to achieve this compensation, the defocusing coefficients must be precisely estimated. According to Eqs. (6) and (13), the compensation of variant quadratic phase errors (expressed by using defocusing coefficients) maximizes this plane component, optimizing the imaging focusing performance.

Essentially, the key to ISAR imaging lies in determining the target in range and azimuth coordinates via the inversion of the received radar echo based on the Doppler analysis. During this signal processing, the phase characteristic plays an irreplaceable role [32]–[35]. In the most ISAR imaging algorithm [36]–[39], the precise phase compensation is performed in azimuth time domain, which aims to estimate the phase error during the pulse compression. Therefore, before the phase compensation, the unfocused RD image  $f(g, h)$  needs to be transformed in azimuth direction through an inverse fast Fourier transform (IFFT) procedure, yielding

$$S(g, l) = \text{IFFT}(f(g, h)) \quad (17)$$

The phase refocusing model is built up with two mutually independent components, the range and azimuth components as follows.

$$S'(g, l) = S(g, l) \times \exp(-i\xi_r gl^2) \quad (18)$$

$$f'(g, h) = \sum_{l=-\frac{L}{2}}^{\frac{L}{2}-1} S'(g, l) \times \exp\left[-i\xi_a hl^2 - \frac{i2\pi hl}{L}\right] \quad (19)$$

where the focusing parameters  $\xi_r$  and  $\xi_a$  are used for the phase compensation in the range and azimuth respectively,  $g = [-\frac{G}{2}, \dots, \frac{G}{2} - 1]$  represents the range position in the RD image,  $h = [-\frac{H}{2}, \dots, \frac{H}{2} - 1]$  represents the Doppler position in the RD image, and  $l = [-\frac{L}{2}, \dots, \frac{L}{2} - 1]$  represents the azimuth time position of the radar echo data, which related to the radar pulse repetition frequency (PRF). It can be calculated by  $l = t_m \cdot \text{PRF}$ , and  $L = H$  in this paper. As shown in Eq. (19), the quadratic azimuth phase compensation needs to be performed with the azimuth compression synchronously because it is related to the azimuth position. In this paper, the discrete Fourier transform (DFT) replaces the conventional FFT procedure so as to avoid generating new phase error in this step.

In order to evaluate the focusing performances of ISAR images before and after the phase compensation, the image entropy is adopted as the image quantitative metric in this work. As widely used in most auto-focusing algorithms [35]–[37], [39], it is expressed as

$$E(f(g, h)) = - \sum_{g=-\frac{G}{2}}^{\frac{G}{2}-1} \sum_{h=-\frac{H}{2}}^{\frac{H}{2}-1} I(g, h) \ln I(g, h) \quad (20)$$

$$I(g, h) = \frac{|f(g, h)|^2}{\sum_{g=-\frac{G}{2}}^{\frac{G}{2}-1} \sum_{h=-\frac{H}{2}}^{\frac{H}{2}-1} |f(g, h)|^2} \quad (21)$$

Then, the refocusing problem is converted into solving an unconstrained minimization of image entropy, thus the focusing parameters,  $\xi_r$  and  $\xi_a$ , are estimated by minimizing the entropy function as

$$\left\{ \hat{\xi}_r, \hat{\xi}_a \right\} = \arg \min_{\xi_r, \xi_a} E(f(g, h; \xi_r, \xi_a)) \quad (22)$$

Since optimization (22) does not have multiple local optima, there are various available algorithms to get its numerical solution, such as the Davidon-Fletcher-Powell (DFP) algorithm and the Broyden-Fletcher-Goldfarb-Shanno (BFGS) algorithm [45]. In this paper, the DFP algorithm (**Algorithm 1**) is adopted and the first-order gradients of the RD image entropy corresponding to the focusing parameters are derived as Eqs. (23)–(28), shown at the bottom of previous page .

Once we obtain the optimal focusing parameters  $\hat{\xi}_r$  and  $\hat{\xi}_a$ , the ISAR image defocusing coefficients  $e_r$  and  $e_a$  are determined as follows.

$$e_r = -\frac{\lambda \text{PRF}^2}{4\pi \Delta r} \hat{\xi}_r \quad (29)$$

$$e_a = \frac{\lambda \text{PRF}^2}{4\pi \Delta f_d} \hat{\xi}_a \quad (30)$$

where  $\Delta r = c/2f_s$  denotes the range pixel resolution of RD images,  $\Delta f_d = \text{PRF}/H$  denotes the Doppler bin resolution of RD images, and  $c$  is the speed of light. Besides, a well-focused ISAR image is also be acquired as the by-product.

#### IV. TARGET DYNAMIC PARAMETER ESTIMATION

Once synchronized four-station phase coefficients are acquired, the target dynamic parameters can be estimated in optimization (16). It should be emphasized that the multiple-station image synchronization refers to synchronizing the central moment of each ISAR image according to the target tracking data, but the CPI duration might vary from one image to another based on the demands of the image azimuth-resolution [24]. The synchronization is based on the GPS time transfer system with  $10^{-3}$  second precision, which ensures the feasibility of the proposed algorithm in practical applications.

In order to solve optimization (16), particle swarm optimization algorithm, one of stochastic intelligent methods, is adopted in this work [40]–[42]. The target dynamic parameters are expressed as the particle positions in the **Algorithm 2**.

$$\chi_i = (\alpha_{Rot}, \Delta\alpha_{Rot}, \beta_{Rot}, \Delta\beta_{Rot})^T \quad (31)$$

The processing of PSO can be summarized as the iterative update of the particle's position and velocity under the guidance of swarm search and particle search experiences. The swarm search aims at finding the best position Gbest in the swarm while the particle search experience inspires to search the best position Pbest in the particle. Relative to the minimization of (16), the subroutines shown in **Algorithm 2** use the fitness function of the dynamic estimation as Eq. (32). The time complexity of the

PSO algorithm adopted is  $O(n^2)$ , and the space complexity is  $O(n)$ .

$$J = \sum_{i=1}^3 \sum_{j=i+1}^4 \left| \vec{v}_T(e_{r,i}, e_{a,i}) \bullet \vec{v}_T(e_{r,j}, e_{a,j}) \right| \quad (32)$$

According to the target dynamic estimation result  $\hat{x} = (\hat{\alpha}_{Rot}, \Delta\hat{\alpha}_{Rot}, \hat{\beta}_{Rot}, \Delta\hat{\beta}_{Rot})^T$  in each image, the normal vector of a plane component is also determined to represent target attitude information by the averaging principle, yielding

$$\vec{v}_T = \frac{1}{4} \sum_{i=1}^4 [e_{r,i}, e_{a,i}, -1]_{1 \times 3} \cdot \mathbf{T}_i \quad (33)$$

Herein, the brief flowchart of the proposed algorithm is depicted in Fig. 2.

#### V. EXPERIMENT ANALYSIS

Due to lacking real measured ISAR data, the capability of the proposed algorithm will be investigated by three simulation experiments in this article.

- At first, a rectangular scattering point array is applied as the observed target to illustrate the feasibility of the proposed algorithm. It should be emphasized that the time synchronization of multiple-station ISAR image is assumed and the

$$\frac{\partial E(f(g, h))}{\partial \xi_r} = - \sum_{g=-\frac{G}{2}}^{\frac{G}{2}-1} \sum_{h=-\frac{H}{2}}^{\frac{H}{2}-1} \left( \frac{\partial I(g, h)}{\partial \xi_r} \text{In}I(g, h) + \frac{\partial I(g, h)}{\partial \xi_r} \right) \quad (23)$$

$$\frac{\partial I(g, h)}{\partial \xi_r} = \frac{\frac{\partial f(g, h) f^*(g, h)}{\partial \xi_r} \times \sum_{g=-\frac{G}{2}}^{\frac{G}{2}-1} \sum_{h=-\frac{H}{2}}^{\frac{H}{2}-1} f(g, h) f^*(g, h) - \sum_{g=-\frac{G}{2}}^{\frac{G}{2}-1} \sum_{h=-\frac{H}{2}}^{\frac{H}{2}-1} \frac{\partial f(g, h) f^*(g, h)}{\partial \xi_r} \times f(g, h) f^*(g, h)}{\left( \sum_{g=-\frac{G}{2}}^{\frac{G}{2}-1} \sum_{h=-\frac{H}{2}}^{\frac{H}{2}-1} f(g, h) f^*(g, h) \right)^2} \quad (24)$$

$$\frac{\partial (f(g, h) f^*(g, h))}{\partial \xi_r} = 2\text{Re} \left( f(g, h) \frac{\partial f^*(g, h)}{\partial \xi_r} \right) = 2\text{Re} \left( f(g, h) i g \sum_{l=-\frac{L}{2}}^{\frac{L}{2}-1} l^2 S^*(g, l) \times \exp \left[ i (\xi_r g + \xi_a h) l^2 + \frac{i 2\pi h l}{L} \right] \right) \quad (25)$$

$$\frac{\partial E(f(g, h))}{\partial \xi_a} = - \sum_{g=-\frac{G}{2}}^{\frac{G}{2}-1} \sum_{h=-\frac{H}{2}}^{\frac{H}{2}-1} \left( \frac{\partial I(g, h)}{\partial \xi_a} \text{In}I(g, h) + \frac{\partial I(g, h)}{\partial \xi_a} \right) \quad (26)$$

$$\frac{\partial I(g, h)}{\partial \xi_a} = \frac{\frac{\partial f(g, h) f^*(g, h)}{\partial \xi_a} \times \sum_{g=-\frac{G}{2}}^{\frac{G}{2}-1} \sum_{h=-\frac{H}{2}}^{\frac{H}{2}-1} f(g, h) f^*(g, h) - \sum_{g=-\frac{G}{2}}^{\frac{G}{2}-1} \sum_{h=-\frac{H}{2}}^{\frac{H}{2}-1} \frac{\partial f(g, h) f^*(g, h)}{\partial \xi_a} \times f(g, h) f^*(g, h)}{\left( \sum_{g=-\frac{G}{2}}^{\frac{G}{2}-1} \sum_{h=-\frac{H}{2}}^{\frac{H}{2}-1} f(g, h) f^*(g, h) \right)^2} \quad (27)$$

$$\frac{\partial (f(g, h) f^*(g, h))}{\partial \xi_a} = 2\text{Re} \left( f(g, h) \frac{\partial f^*(g, h)}{\partial \xi_a} \right) = 2\text{Re} \left( f(g, h) i h \sum_{l=-\frac{L}{2}}^{\frac{L}{2}-1} l^2 S^*(g, l) \times \exp \left[ i (\xi_r g + \xi_a h) l^2 + \frac{i 2\pi h l}{L} \right] \right) \quad (28)$$

where \* refers to the conjugation.

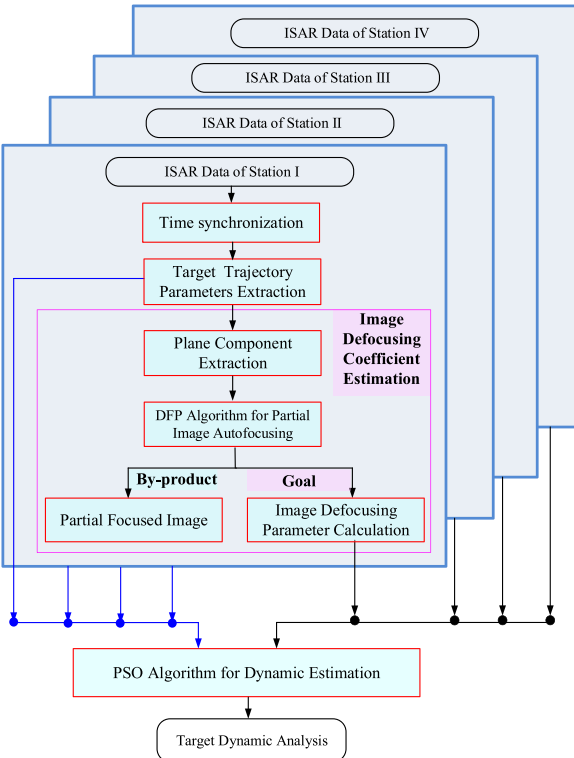


Fig. 2. The flowchart of the proposed algorithm.

TABLE I  
THE MAIN PARAMETERS OF THE ISAR SYSTEM

Size of a single image	$256 \times 512$
Wave length of the signal	0.018 m
Bandwidth	750 MHz
Center frequency of the transmit signal	16.7 GHz
Pulse repetition frequency	50 Hz
Sample frequency	1.5 GHz

target translation is well compensated in the RD imaging according to the target tracking data.

- Then, the Aura satellite as a typical satellite target replaces former scattering point array for dynamic estimation to validate the effectiveness of the proposed algorithm in different target attitude conditions. And the anti-noise jamming experiment is also given to demonstrate the steadiness of the proposed algorithm.
- In the end, the dynamic estimation performance of the proposed algorithm is compared with that of the existing algorithm in Ref. [24]. The comparison results illustrate the progress of the proposed algorithm in dynamic estimation of spin targets.

The main parameters of ISAR system are given in Table I, and the location coordinates of four ground-based observation stations are given in Table II. The 3D model of the Aura satellite is depicted in Fig. 3, and target two-line-element (TLE) parameters are adopted with a low earth orbit (LEO) satellite at the altitude of 400 km. The point-like simulation strategy is applied

TABLE II  
THE LOCATION COORDINATES OF ISAR STATIONS

Station 1	(39.9 N, 116.3 E, 88 m)
Station 2	(39.1 N, 117.1 E, 33 m)
Station 3	(38.2 N, 114.7 E, 77 m)
Station 4	(39.0 N, 113.3 E, 11 m)

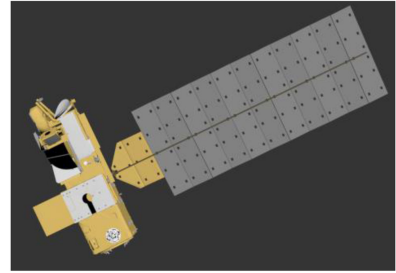


Fig. 3. The 3D model of TG-I Spacecraft.

to calculate signal echo in Part A, while the improved physical optical algorithm is adopted to calculate radar echo according to the target facet model in Part B and Part C [46].

#### A. Demonstration Experiments With a Planar Scattering Point Array

In this part, the capability of the proposed dynamic estimation algorithm is investigated with the point-like simulation images of a spin plane component composed of a rectangle scattering point array. The instantaneous dynamic parameters of the target are given in the second column of Table III. At this moment, the spin target is projected with different poses in these four imaging planes, as shown in the first column of Fig. 4. And the defocusing of scatter points displays a symmetrical distribution around the scene center in all these ISAR images, which exactly coincides with the quadratic phase error presentation in Eq. (13). According to the proposed algorithm, the refocusing coefficients in each image are estimated via the DFP algorithm. As shown in the second column of Fig. 4, the image entropy gradually decreases during the refocusing processing, and then the well-focused images are also obtained as shown in the third column of Fig. 4.

With the image refocusing coefficients determined, target dynamic parameters ( $\alpha_{Rot}$ ,  $\Delta\alpha_{Rot}$ ,  $\beta_{Rot}$ ,  $\Delta\beta_{Rot}$ ) are estimated through Eq. (16). At last, the instantaneous attitude of the target, i.e. the normal vector of the plane component, is solved according to Eq. (33) and we can also calculate the target spin speed  $\omega = \sqrt{\alpha_{Rot}^2 + \beta_{Rot}^2}$ . As listed in Table III, the estimated results of the target dynamic parameters are compared with the true values of them, and the comparison illustrates the accuracy of the proposed algorithm.

#### B. Demonstration Experiments With a Typical Satellite

Following the previous experiment, the Aura satellite is applied to validate the feasibility of the proposed algorithm in practical applications. Four original ISAR images are given in

TABLE III  
THE TARGET DYNAMIC ESTIMATION RESULTS

Parameters	True value	Estimation result	Error
$\alpha_{\text{Rot}}$	$9.0 \times 10^{-3} \text{ rad/s}$	$8.7 \times 10^{-3} \text{ rad/s}$	$3.0 \times 10^{-4} \text{ rad/s}$
$\beta_{\text{Rot}}$	$5.0 \times 10^{-3} \text{ rad/s}$	$4.2 \times 10^{-3} \text{ rad/s}$	$8.0 \times 10^{-4} \text{ rad/s}$
$\Delta\alpha_{\text{Rot}}$	$2.7 \times 10^{-4} \text{ rad/s}^2$	$2.6 \times 10^{-4} \text{ rad/s}^2$	$0.1 \times 10^{-4} \text{ rad/s}^2$
$\Delta\beta_{\text{Rot}}$	$1.5 \times 10^{-4} \text{ rad/s}^2$	$1.2 \times 10^{-4} \text{ rad/s}^2$	$0.3 \times 10^{-4} \text{ rad/s}^2$
The normal vector of the plane component	(0.3420, -0.9397, 0)	(-0.3405, 0.9368, -0.0738)	2.96 degrees
Target spin speed	$1.03 \times 10^{-2} \text{ rad/s}$	$9.8 \times 10^{-3} \text{ rad/s}$	$5.0 \times 10^{-4} \text{ rad/s}$

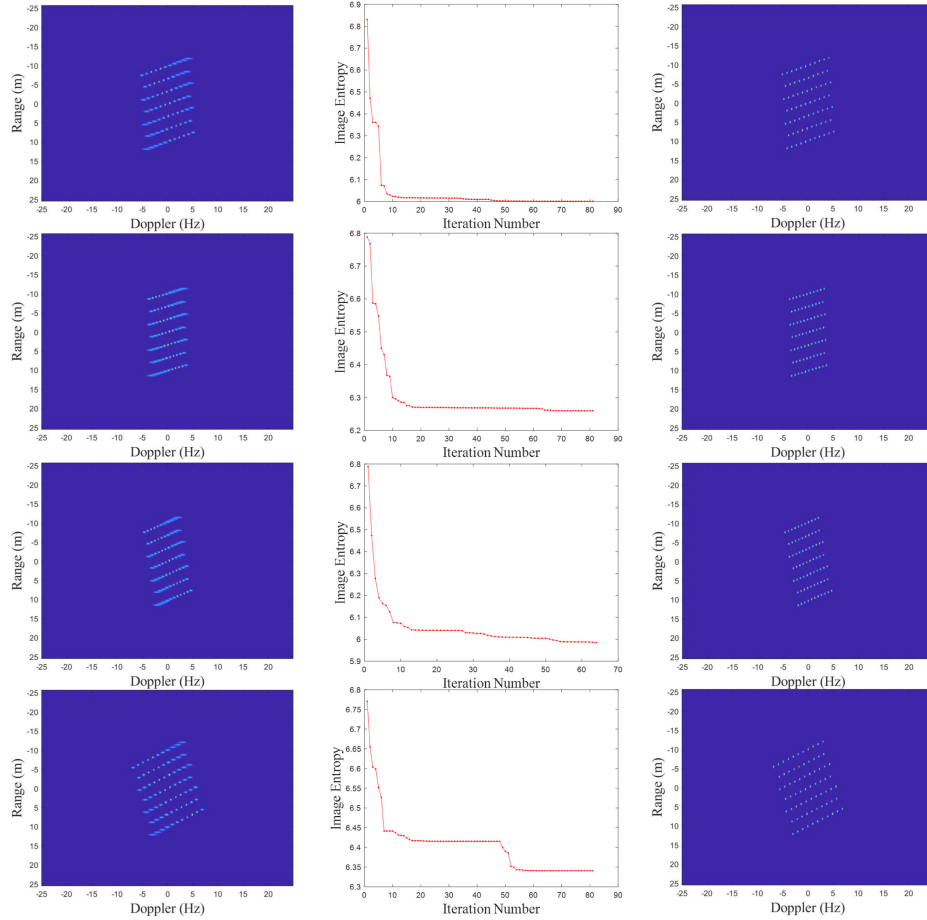


Fig. 4. The refocusing results of the point-like simulation images (First column: Original ISAR images; Second column: Image entropy change during the refocusing processing; Third column: Well-focused ISAR images after image refocusing).

the first column in Fig. 5. As the proposed algorithm is based on the phase characteristics of the plane component, the solar wing part in the Aura satellite ought to be segmented from the ISAR image in advance. A simple but effective method for this segmentation is performed through judging whether the points are located between the two sets of given opposite sides or not [24]. Then, by using the proposed image refocusing algorithm, each image quality has been improved as shown in the third column in Fig. 5. Particularly for the solar wing part, the entropy of this fraction decreases to the minimum, and the visible difference exists between the second column and fourth

column in Fig. 5. Besides, the focusing performances of the other parts (marked yellow) in the entire image also are enhanced.

With these defocusing coefficients obtained, the target dynamic parameters can be estimated according to Eq. (16). As listed in Table IV, the estimated results of dynamic parameters are close to the true values. According to the estimation results, the visualization of target motion is shown in Fig. 6, where the expected target dynamic information are plotted in the target Cartesian coordinates. Besides, the imaging planes defined by the target trajectory and spin motion can also be determined further supporting the analysis for the target dynamic state in the practical application.

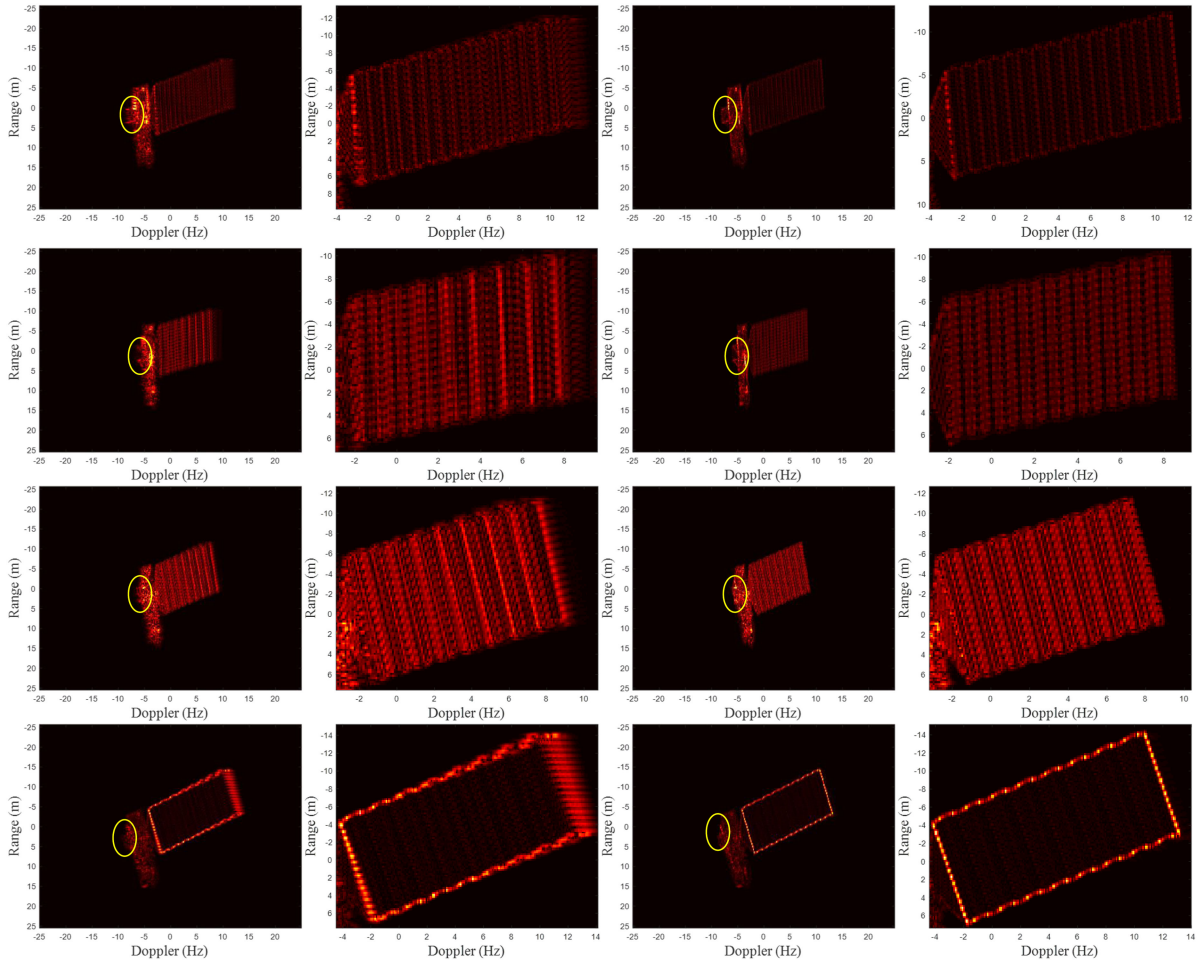


Fig. 5. The refocusing results of the Aura satellite(First column: Original ISAR images; Second column: Partial images of the plane component in original ISAR images; Third column: Well-focused ISAR images; Fourth column after image refocusing: Partial images of the plane component in well-focused ISAR images).

TABLE IV  
THE TARGET DYNAMIC ESTIMATION RESULTS OF AURA

Parameters	True value	Estimation result	Error
$\alpha_{\text{Rot}}$	$9.0 \times 10^{-3} \text{ rad/s}$	$9.0 \times 10^{-3} \text{ rad/s}$	0
$\beta_{\text{Rot}}$	$5.0 \times 10^{-3} \text{ rad/s}$	$4.2 \times 10^{-3} \text{ rad/s}$	$8.0 \times 10^{-4} \text{ rad/s}$
$\Delta\alpha_{\text{Rot}}$	$2.4 \times 10^{-4} \text{ rad/s}^2$	$2.7 \times 10^{-4} \text{ rad/s}^2$	$0.3 \times 10^{-4} \text{ rad/s}^2$
$\Delta\beta_{\text{Rot}}$	$1.5 \times 10^{-4} \text{ rad/s}^2$	$2.5 \times 10^{-4} \text{ rad/s}^2$	$1.0 \times 10^{-4} \text{ rad/s}^2$
The normal vector of the plane component	(-0.6428, 0.7660, 0)	(-0.6658, 0.7448, -0.0440)	3.09 degrees
Target spin speed	$1.03 \times 10^{-2} \text{ rad/s}$	$9.9 \times 10^{-3} \text{ rad/s}$	$4.0 \times 10^{-4} \text{ rad/s}$

Furthermore, in order to demonstrate the feasibility and accuracy of the proposed algorithm in the practical application, two more experiments are designed. At first, the pose of the Aura satellite varies along the trajectory and the proposed algorithm is repeated to illustrate its feasibility. Similar to the previous experiment, the image refocusing and dynamic estimation results are given in Fig. 7 and Table V, respectively. It is shown that the experiment results confirm its feasibility.

Then, the target dynamic estimation experiment is repeated on the additive white Gaussian noise background to investigate the proposed algorithm sensitivity to random noise. In this paper,

the signal-to-noise ratio (SNR) of a signal is defined as

$$\text{SNR} = 10 \log_{10} (E_s / E_n) \quad (34)$$

where  $E_s$  denotes the energy of radar echo, and  $E_n$  denotes the energy of white Gaussian noise.

The estimation error curves of target attitude and target spin speed are given in Table VI. In the experiments under two different pose conditions, the proposed algorithm keeps the high-precision for the target dynamic estimation with the SNR

TABLE V  
THE TARGET DYNAMIC ESTIMATION RESULTS OF AURA IN ANOTHER POSE

Parameters	True value	Estimation result	Error
$\alpha_{\text{Rot}}$	$9.0 \times 10^{-3} \text{ rad/s}$	$8.8 \times 10^{-3} \text{ rad/s}$	$2.0 \times 10^{-4} \text{ rad/s}$
$\beta_{\text{Rot}}$	$5.0 \times 10^{-3} \text{ rad/s}$	$4.8 \times 10^{-3} \text{ rad/s}$	$2.0 \times 10^{-4} \text{ rad/s}$
$\Delta\alpha_{\text{Rot}}$	$2.7 \times 10^{-4} \text{ rad/s}^2$	$2.6 \times 10^{-4} \text{ rad/s}^2$	$0.1 \times 10^{-4} \text{ rad/s}^2$
$\Delta\beta_{\text{Rot}}$	$1.5 \times 10^{-4} \text{ rad/s}^2$	$1.4 \times 10^{-4} \text{ rad/s}^2$	$0.1 \times 10^{-4} \text{ rad/s}^2$
The normal vector of the plane component	(0.3420, -0.9397, 0)	(-0.3405, 0.9368, -0.0738)	4.24 degrees
Target spin speed	$1.03 \times 10^{-2} \text{ rad/s}$	$9.4 \times 10^{-3} \text{ rad/s}$	$9.0 \times 10^{-4} \text{ rad/s}$

TABLE VI  
THE TARGET DYNAMIC ESTIMATION ERRORS IN DIFFERENT SNR CONDITIONS

SNR(dB)	-12	-8	-4	0	4	8	12	16	20
Pose I									
Target attitude vector error (degrees)	50.07	7.40	5.13	3.12	3.44	3.43	3.57	3.51	3.51
Target spin speed error ( $\times 10^{-3} \text{ rad/s}$ )	4.7	2.4	2.4	2.2	1.3	1.1	1.2	0.8	0.4
Pose II									
Target attitude vector error (degrees)	13.23	10.77	4.06	4.14	4.67	4.12	4.70	4.40	4.73
Target spin speed error ( $\times 10^{-3} \text{ rad/s}$ )	3.4	2.4	2.0	1.8	1.6	1.3	1.3	1.1	0.9

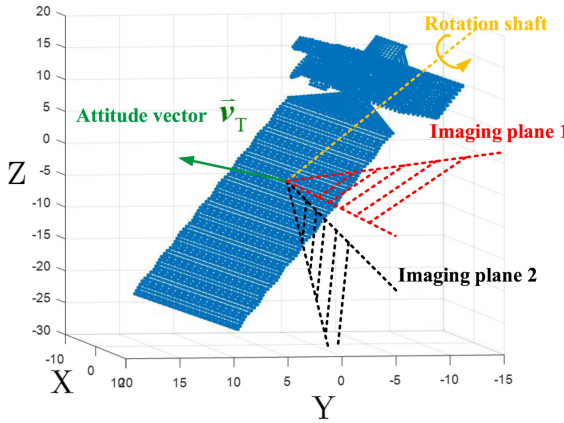


Fig. 6. The instantaneous motion analysis of Aura satellite.

changing. Even when the SNR decreases to -4 dB, the error of plane pointing is around 5 degrees and target spin speed is near its true value, proving the robustness of the proposed algorithm against noise and jamming.

### C. Comparison Experiments

In order to illustrate the superiority of the proposed algorithm, the performance of the proposed method is compared with that of the existing estimation method in Ref. [24], which also uses image defocusing coefficients to analyze the attitude information of attitude-stabilized satellites. In this experiment, it is assumed that the target attitude is spinning at 0.015 rad/s and the observation conditions of these two algorithms are identical. As shown in Fig. 8, four ISAR images are simultaneously generated according to the observation geometry. Through the proposed refocusing method, the defocusing coefficients of these images are obtained. Then, these parameters are applied to achieve

the dynamic estimation of the target in the two algorithms respectively, and their estimation performances are compared in a quantitative way. From the estimation results in Table VII, the target attitude precision of the proposed estimation algorithm is higher than that of the existing algorithm in [24] as it takes the target spin motion into consideration. Moreover, it draws the accurate parameters of the target spin motion, while the existing method fails. In other words, the proposed algorithm breaks through the constraint of the target stability state assumption which is the basis of performing some conventional algorithms in current references [18], [22], [23]. As a result, the proposed algorithm can be adopted for the dynamic estimation of most in-orbit satellites. Compared to existing methods, this approach requires only the additional element, multiple-stage image synchronization, to improve its estimation performance. Based on the GPS time transfer system, this demand can be ensured in most multiple-station radar imaging scenes [10], [30]–[33]. Therefore, the superiority of the proposed is demonstrated by this comparison experiment.

### D. Discussion of the Results

All in all, the above experiment results illustrate the superiority of the proposed methods, but there remain some limitations which impact the usability of the dynamic estimation in practical applications.

The one constraint derives from the projection shape of the plane component in the image which depends on both the observation angle of the ground radar and target spin motion. In some cases, the plane component will be projected as a thin polygon, decreasing the precision of extracted phase coefficients. As the propagation of this error, finally the dynamic estimation results might not become acceptable. For avoiding this problem in

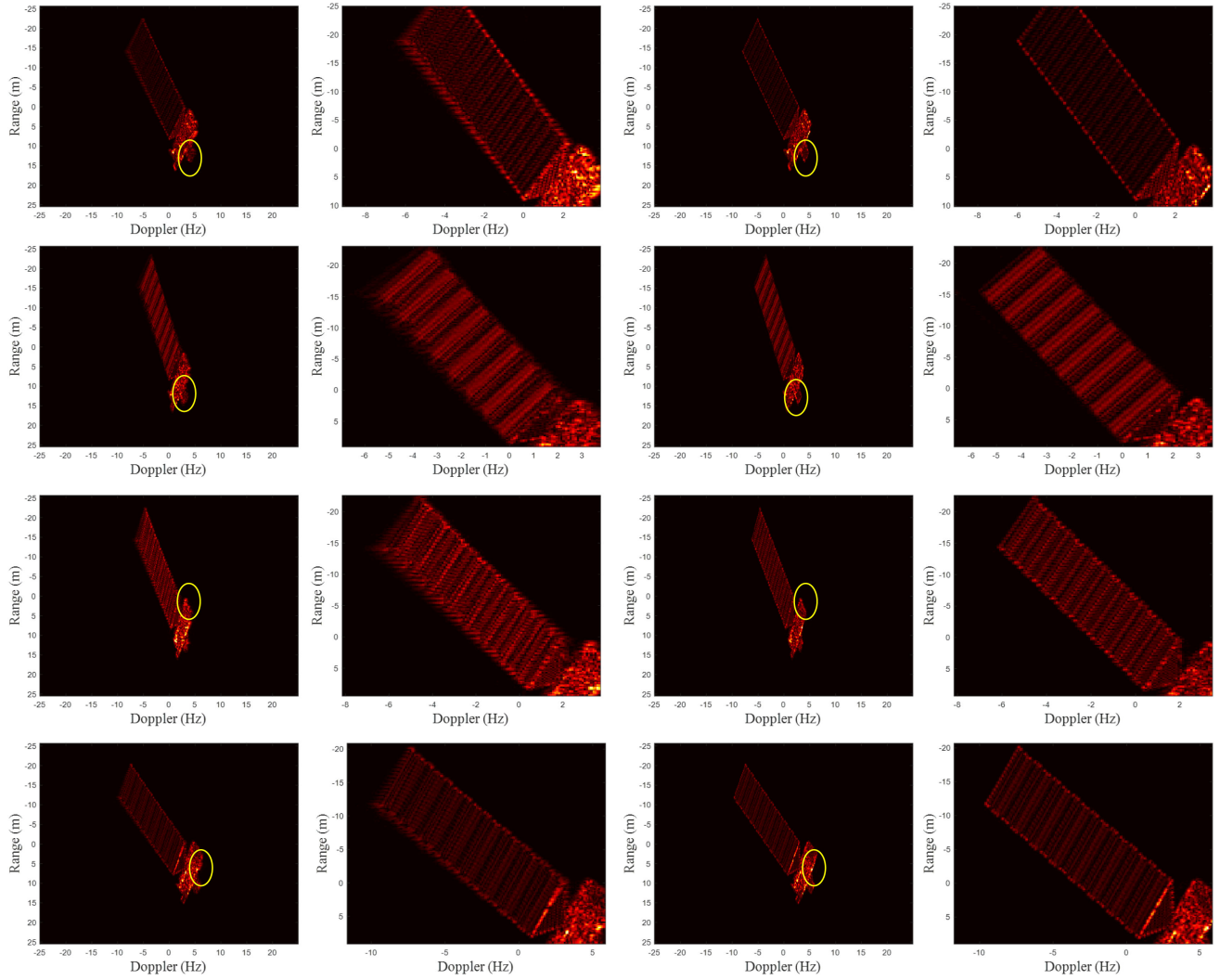


Fig. 7. The refocusing results of the Aura satellite in another pose (First column: Original ISAR images; Second column: Partial images of the plane component in original ISAR images; Third column: Well-focused ISAR images; Fourth column after image refocusing: Partial images of the plane component in well-focused ISAR images).

TABLE VII  
THE PERFORMANCE COMPARISON BETWEEN THE PROPOSED ALGORITHM AND EXISTING METHOD

Method		The proposed method		The existing method	
Parameters	True value	Estimation result	Error	Estimation result	Error
$\alpha_{\text{Rot}}$	$1.2 \times 10^{-2} \text{ rad/s}$	$1.16 \times 10^{-2} \text{ rad/s}$	$4.0 \times 10^{-4} \text{ rad/s}$	0	-
$\beta_{\text{Rot}}$	$8.0 \times 10^{-3} \text{ rad/s}$	$7.6 \times 10^{-2} \text{ rad/s}$	$4.0 \times 10^{-4} \text{ rad/s}$	0	-
$\Delta\alpha_{\text{Rot}}$	$3.6 \times 10^{-4} \text{ rad/s}^2$	$3.48 \times 10^{-4} \text{ rad/s}^2$	$0.12 \times 10^{-4} \text{ rad/s}^2$	0	-
$\Delta\beta_{\text{Rot}}$	$2.4 \times 10^{-4} \text{ rad/s}^2$	$2.28 \times 10^{-4} \text{ rad/s}^2$	$0.12 \times 10^{-4} \text{ rad/s}^2$	0	-
The normal vector of the plane component	(0.3420, -0.9397, 0)	(-0.3627, 0.9237, -0.0908)	5.42 degrees	(-0.3662, 0.8440, -0.1993)	12.69 degrees
Target spin speed	$1.5 \times 10^{-2} \text{ rad/s}$	$1.39 \times 10^{-2} \text{ rad/s}$	$1.1 \times 10^{-3} \text{ rad/s}$	0	-

practical application, it proves effective to increase the number of observation stations when the projection area of the plane component is too small in some of multiple-station images. In general, when the LOS intersection angle scope relative to multiple-station imaging plane is large enough, it is easier to get

an ideal estimation performance. However, it is hard to draw an explicit expression of the position design of the multiple-station system due to the diversity of the observation geometry, which needs to be further investigated in the future work.

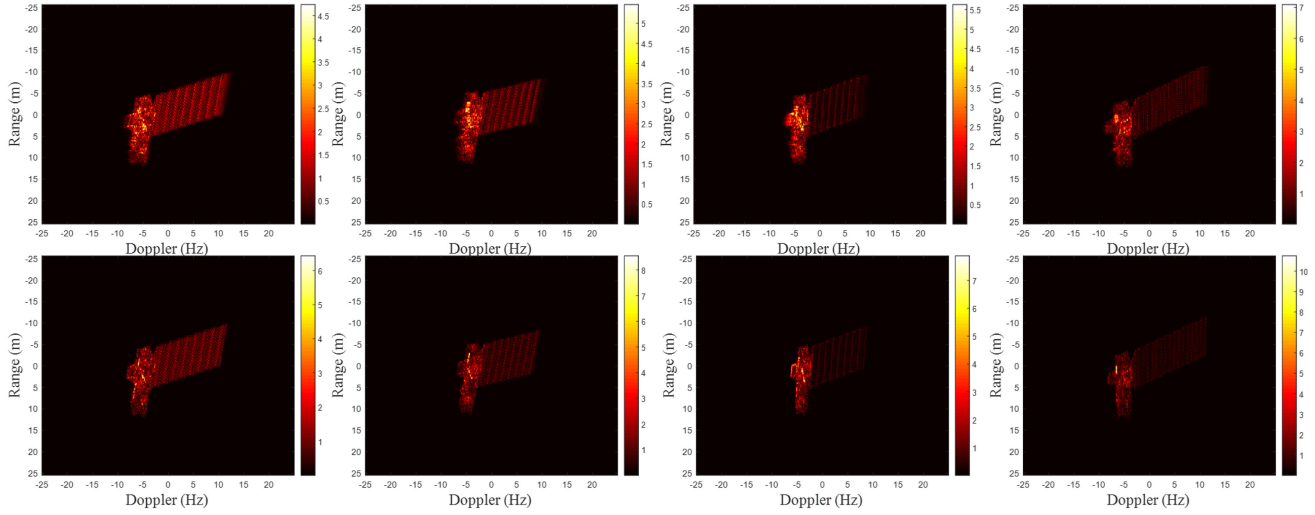


Fig. 8. The refocusing results of the Aura satellite in the comparison experiment (First row: original ISAR images; Second row: well-focused ISAR images after the refocusing processing).

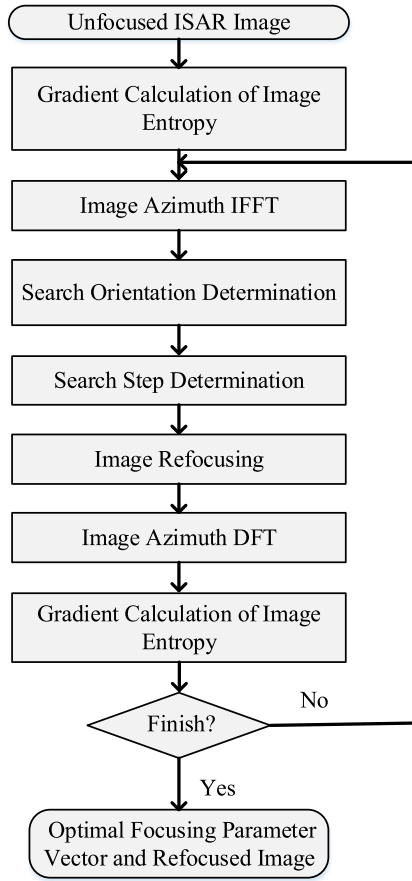


Fig. 9. The flowchart of Algorithm 1.

The other is the height of the target orbit. For high orbit targets, the change speed of the elevation angle usually is inadequate to match up with that of the azimuth angle in the ground observation. As a result, the defocusing characteristics are imbalanced in the two dimensions of the ISAR image even without the

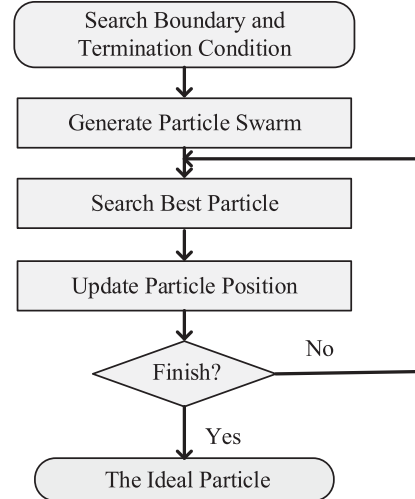


Fig. 10. The flowchart of Algorithm 2.

consideration of the target spin motion. One of the conclusions of the experiment is that the ratio of angular speeds ought to be less than 8 in these two dimensions. Therefore, the application scope of the proposed algorithm is bounded by the condition that the height orbit of satellites should be no more than 1000 km. Besides, the main subjects in this work are LEO satellites, and thus other spin space targets such as space debris are not taken into consideration due to the difficulty of obtaining their high-resolution images.

## VI. CONCLUSION

In this paper, an approach was presented to interpret the phase characteristic in multiple-station ISAR images so as to estimate the dynamic parameters of spin in-orbit satellites. Through analyzing the relationship between the image defocusing coefficient and target spin motion, an explicit expression about this relation

**Algorithm 1:** ISAR Image Refocusing.

---

**Input :**

- the unfocused image:  $f_0(g, h)$
- gradient threshold:  $\varepsilon$

/\* Parameters Initialization \*/

- 1 focusing parameters vector:  $\vec{\xi}_0 = (\xi_{r,0}, \xi_{a,0})^T = (0, 0)^T$
- 2 Hessian matrix:  $\mathbf{D}_0 = \mathbf{E}$
- 3 iteration number:  $j = 1$

/\* DFP Algorithm for Phase Coefficient Estimation \*/

- 4 while  $\|\vec{\mathbf{g}}_{j+1}\| > \varepsilon$  do
- 5   Computer  $\vec{\mathbf{g}}_j = \left( \frac{\partial E(f_{j-1}(g, h; \{\xi_{r,j-1}, \xi_{a,j-1}\}))}{\partial \xi_{r,j-1}}, \frac{\partial E(f_{j-1}(g, h; \{\xi_{r,j-1}, \xi_{a,j-1}\}))}{\partial \xi_{a,j-1}} \right)^T$  according to Eqs. (23)-(28)
- 6    $\vec{\mathbf{d}}_j = -\mathbf{D}_{j-1} \cdot \vec{\mathbf{g}}_j$
- 7   Solve  $\lambda_j = \arg \min_{\lambda \in R} E(f_{j-1}(g, h; \vec{\xi}_{j-1} + \lambda \vec{\mathbf{d}}_j))$  by the one-dimensional inexact searching method
- 8    $\vec{\mathbf{s}}_j = \lambda_j \vec{\mathbf{d}}_j$
- 9    $\vec{\xi}_j = \vec{\xi}_{j-1} + \vec{\mathbf{s}}_j$
- 10   Substitute  $\vec{\xi}_j$  into Eqs. (18)-(19) to compensate the phase error
- 11   Computer  $\vec{\mathbf{g}}_{j+1}$  according to the compensated image  $f_j(g, h)$
- 12    $\vec{\mathbf{y}}_j = \vec{\mathbf{g}}_{j+1} - \vec{\mathbf{g}}_j$
- 13    $\mathbf{D}_j = \mathbf{D}_{j-1} + \frac{\vec{\mathbf{s}}_j \vec{\mathbf{s}}_j^T}{\vec{\mathbf{s}}_j^T \vec{\mathbf{y}}_j} - \frac{\mathbf{D}_{j-1} \vec{\mathbf{y}}_j \vec{\mathbf{y}}_j^T}{\vec{\mathbf{y}}_j^T \mathbf{D}_{j-1} \vec{\mathbf{y}}_j}$
- 14    $j = j + 1$
- 15 end

/\* Focusing Parameter Determination \*/

- 16  $\left( \hat{\xi}_r, \hat{\xi}_a \right)^T = \sum_{q=1}^j \vec{\xi}_q$

**Output:**

- optimal focusing parameter vector:  $(\hat{\xi}_r, \hat{\xi}_a)^T$
- refocused image:  $f_j(g, h)$

---

**Algorithm 2:** PSO Algorithm for Target Parameter Estimation.

---

**Input :**

- the search boundary of the optimization (16):  $\varpi$
- the maximum iteration:  $\varepsilon_1$
- minimum move distance:  $\varepsilon_2$

/\* Parameters Initialization \*/

- 1 Randomly generate a particle swarm  $\Lambda$  according to  $\varpi$
- 2 inertia weight:  $a_0 = 0.6$
- 3 learning rate weight:  $a_1 = 0.7$
- 4 learning rate weight:  $a_2 = 0.9$
- 5 iteration number:  $j = 1$

/\* PSO Algorithm \*/

- 6 while  $\vec{\delta}_i(j+1) \geq \varepsilon_1$  or  $j = \varepsilon_2$  do
- 7   for  $\vec{\chi}_i(j) \in \Lambda$  do
- 8     if  $J(\vec{\chi}_i) \leq Pbest$  then
- 9        $Pbest = J(\vec{\chi}_i)$
- 10     end
- 11     if  $Pbest \leq Gbest$  then
- 12        $Gbest = Pbest$
- 13     end
- 14   end
- 15   /\* Swarm Update \*/
- 16   for Randomly generate  $rand_1, rand_2$  uniformly distributed within  $[0, 1]$
- 17      $\vec{\chi}_i(j) \in \Lambda$  do
- 18        $\vec{\delta}_i(j+1) = a_0 \vec{\delta}_i(j) + a_1 rand_1 (Pbest - \vec{\chi}_i(j)) + a_2 rand_2 (Gbest - \vec{\chi}_i(j))$
- 19        $\vec{\chi}_i(j+1) = \vec{\chi}_i(j) + \vec{\delta}_i(j)$
- 20     end
- 21    $j = j + 1$
- 22 Find the ideal particle  $\hat{\chi}$  in current swarm

**Output:**

- the ideal particle:  $\hat{\chi}$

---

TABLE VIII  
MAIN MATHEMATICAL SYMBOLS USED IN THIS PAPER

Symbols	Annotation
$S(\tau, t_m)$	radar echo
$R_p(t_m)$	slant-range of the scattering point
$\vec{p}(x, y, z)$	scattering center position
$\vec{k}(\theta(t_m), \phi(t_m))$	instantaneous LOS unit vector
$(\alpha_{\text{Tra}}, \Delta\alpha_{\text{Tra}}, \beta_{\text{Tra}}, \Delta\beta_{\text{Tra}})$	target trajectory parameters
$(\alpha_{\text{Rot}}, \Delta\alpha_{\text{Rot}}, \beta_{\text{Rot}}, \Delta\beta_{\text{Rot}})$	target spin parameters
$\Omega$	a plane component
$\vec{v}_T$	normal vector of the plane component
$f(g, h)$	unfocused RD image
$(e_r, e_a)$	image defocusing coefficients
$E(f(g, h))$	image entropy
$(\hat{\xi}_r, \hat{\xi}_a)$	image focusing parameters
$f'(g, h)$	refocused RD image

was derived. An image autofocusing algorithm was adopted to acquire the defocusing coefficients in the multiple-station images, and then these coefficients were directly applied to build the optimization of the target dynamic estimation which was solved by the PSO algorithm. The experiment results have confirmed the effectiveness of the proposed algorithm. Compared with the existing methods, the instantaneous dynamic parameters of most in-orbit satellites can be obtained through the proposed method regardless of the target stability state assumption. We believe this work offers an effective approach to accomplish satellite dynamic estimation and also presents a new perspective that the defocusing characteristics of ISAR image is not always an unexpected phenomenon but also an important feature in the image interpretation. For a certain in-orbit satellite in practical applications, the position distribution of the multiple-station system determines the manifold of the proposed optimization, and its impact on the precision of the parameter estimation also needs to be further investigated in the future work.

#### ACKNOWLEDGMENT

The authors thank the anonymous reviewers for their valuable comments to improve the paper quality.

#### APPENDIX

In the Appendices Part, the main mathematical symbols used in the paper are listed in Table VIII, and the flowcharts and pseudocodes of **Algorithm 1** and **Algorithm 2** are also provided.

#### REFERENCES

- [1] N. Bobrinsky, L. Monte, "The space situational awareness program of the European Space Agency," *Cosmic Res.*, vol. 48, no. 5, pp. 392–398, 2010.
- [2] *Haystack Ultrawideband Satellite Imaging Radar*, MIT Lincoln Lab, Lexington, MA, USA, Sep. 2014.
- [3] R. Xu *et al.*, "Exploration of blockchain-enabled decentralized capability-based access control strategy for space situation awareness," *Opt. Eng.*, vol. 58, no. 4, 2019, Art. no. 041609.
- [4] R. Teehan, "Responsive space situation awareness in 2020," Air War Coll Maxwell Center for Strategy and Technology, Tech. Rep., 2007, pp. 1–47.
- [5] Z. Qian, O. Abdel-Rahman, H. Al-Atrash, and I. Batarseh, "Modeling and control of three-port DC/DC converter interface for satellite applications," *IEEE Trans. Power Electron.*, vol. 25, no. 3, pp. 637–649, Mar. 2009.
- [6] *Spacecraft Attitude Determination and Control*, vol. 73, J. R. Wertz, ed. Berlin, Germany: Springer Science and Business Media, pp. 410–459, 2012.
- [7] T. Kouyama, A. Kanemura, S. Kato and *et al.*, "Satellite attitude determination and map projection based on robust image matching," *Remote Sens.*, vol. 9, no. 90, pp. 1–20, 2017.
- [8] D. Kucharski *et al.*, "Attitude and spin period of space debris envisat measured by satellite laser ranging," *IEEE Trans. Geosci. Remote Sens.*, vol. 52, no. 12, pp. 7651–7657, Dec. 2014.
- [9] J. Pittet, J. Silha, T. Schildknecht, "Spin motion determination of the Envisat satellite through laser ranging measurements from a single pass measured by a single station," *Adv. Space Res.*, vol. 64, no. 4, pp. 1–11, 2018.
- [10] Y. Zhou, L. Zhang, Y. Cao, and Y. Huang, "Optical-and-radar image fusion for dynamic estimation of spin satellites," *IEEE Trans. Imag. Process.*, vol. 29, pp. 2963–2976, Jan. 2020.
- [11] G. Kirchner, W. Hausleitner, E. Cristea, "Ajisai spin parameter determination using Graz kilohertz satellite laser ranging data," *IEEE Trans. Geosci. Remote Sens.*, vol. 45, no. 1, pp. 201–205, Jan. 2007.
- [12] P. Huang, X. Xia, X. Liu, and G. Liao, "Refocusing and motion parameter estimation for ground moving targets based on improved axis rotation-time reversal transform," *IEEE Trans. Comput. Imag.*, vol. 4, no. 3, pp. 479–494, Sep. 2018.
- [13] S. Amico, M. Benn, J. Jorgensen, "Pose estimation of an uncooperative spacecraft from actual space imagery," *Int. J. Space Sci. Eng.*, vol. 5, no. 2, pp. 171–189, 2013.
- [14] R. Perrier, E. Arnaud, P. Sturm, and M. Ortner, "Satellite image registration for attitude estimation with a constrained polynomial model," in *Proc. IEEE Int. Conf. Image Process.*, 2010, pp. 925–928.
- [15] R. Kanzler *et al.*, "Space debris attitude simulation—IOTA (In-Orbit Tumbling Analysis)," in *Proc. Adv. Maui Opt. Space Surveillance Technol. Conf.*, 2015, pp. 1–13.
- [16] L. Yang *et al.*, "A 3-D Electromagnetic-model-based algorithm for absolute attitude measurement using wideband radar," *IEEE Geosci. Remote Sens. Lett.*, vol. 12, no. 9, pp. 1878–1882, Sep. 2015.
- [17] G. Li, J. Zou, S. Xu and *et al.*, "A method of 3D reconstruction via ISAR sequences based on scattering centers association for space rigid object," in *Proc. SPIE Secur. Defence. Int. Soc. Opt. Photon.*, 2014, pp. 1–6.
- [18] W. Zhong, J. Ji, X. Lei, "The attitude estimation of three-axis stabilized satellites using hybrid particle swarm optimization combined with radar cross section precise prediction," *Proc. Inst. Mech. Eng. Part G, J. Aerosp. Eng.*, vol. 31, no. 2, pp. 222–224, 2015.
- [19] S. Lemmens, H. Krag, and J. Rosebrock, "Radar mappings for attitude analysis of objects in orbit," in *Proc. 6th Eur. Conf. Space Debris*, 2013, pp. 20–24.
- [20] S. Lemmens, and H. Krag, "Sensitivity of automated attitude determination form ISAR radar mappings," in *Proc. Adv. Maui Opt. Space Surveillance. Technol. Conf.*, 2013, pp. 1–12.
- [21] J. Rosebrock, "Absolute attitude from monostatic radar measurements of rotating Objects," *IEEE Trans. Geosci. Remote Sens.*, vol. 49, no. 10, pp. 3737–3744, Oct. 2011.
- [22] K. Suwa, T. Wakayama, and M. Iwamoto, "Three-dimensional target geometry and target motion estimation method using multistatic ISAR movies and its performance," *IEEE Trans. Geosci. Remote Sens.*, vol. 49, no. 6, pp. 2361–2373, Jun. 2011.
- [23] Y. Zhou , L. Zhang , Y. Cao, and Z. Wu, "Attitude estimation and geometry reconstruction of satellite targets based on ISAR image sequence interpretation," *IEEE Trans. Aerosp. Electron. Syst.*, vol. 55, no. 4, pp. 1698–1711, Aug. 2019.
- [24] Y. Zhou , L. Zhang and Y. Cao, "Attitude estimation for space targets by exploiting quadratic phase parameters of inverse synthetic aperture radar imagery," *IEEE Trans. Geosci. Remote Sens.*, vol. 57, no. 6, pp. 3858–3872, Jun. 2019.
- [25] F. Santi, D. Pastina, M. Bucciarelli, "Estimation of ship dynamics with a multi-platform radar imaging system," *IEEE Trans. Aerosp. Electron. Syst.*, vol. 53, no. 6, pp. 2769–2788, Dec. 2017.
- [26] F. Santi, M. Bucciarelli, and D. Pastina, "Target rotation motion estimation from distributed ISAR data," in *Proc. IEEE Radar Conf.*, 2012, pp. 1–6.
- [27] C. Yeh *et al.*, "Rotational motion estimation for ISAR via triangle pose difference on two range-Doppler images," *IET Radar, Sonar Navigation*, vol. 4, no. 4, pp. 528–536, 2010.

- [28] C. Yeh, J. Yang, Y. Peng, and X. Shan, "Rotation estimation for ISAR targets with a spaceCtime analysis technique," *IEEE Geosci. Remote Sens. Lett.*, vol. 8, no. 5, pp. 899–903, Sep. 2011.
- [29] S. Brisken, M. Martorella, T. Maty C. Wasserzier, J. G. Worms, and J. H. G. Ender, "Motion estimation and imaging with a multistatic ISAR system," *IEEE Trans. Aerosp. Electron. Syst.*, vol. 50, no. 3, pp. 1701–1714, Jul. 2014.
- [30] D. Pastina, B. Marta, and L. Pierfrancesco, "Multistatic and MIMO distributed ISAR for enhanced cross-range resolution of rotating targets," *IEEE Trans. Geosci. Remote Sens.*, vol. 48, no. 8, pp. 3300–3317, Aug. 2010.
- [31] H. Mansour, D. Liu, U. Kamilov, and P. T. Boufounos, "Sparse blind deconvolution for distributed radar autofocus imaging," *IEEE Trans. Comput. Imag.*, vol. 4, no. 4, pp. 537–551, Dec. 2018.
- [32] Z. She, and Y. Liu, "Autofocus for ISAR imaging using higher order statistics," *IEEE Geosci. Remote Sens. Lett.*, vol. 5, no. 2, pp. 299–303, Apr. 2008.
- [33] S. Brisken *et al.*, "Multistatic ISAR autofocussing using image contrast optimization," in *Proc. IET Int. Conf. Radar Syst. (Radar 2012)*, 2012, pp. 1–4.
- [34] G. Xu, L. Yang, G. Bi and M. Xing, "Enhanced ISAR imaging and motion estimation with parametric and dynamic sparse Bayesian learning," *IEEE Trans. Comput. Imag.*, vol. 3, no. 4, pp. 940–952, Dec. 2017.
- [35] S. Agaian, S. Blair, and A. Karen, "Transform coefficient histogram-based image enhancement algorithms using contrast entropy," *IEEE Trans. Image Process.*, vol. 16, no. 3, pp. 741–758, Mar. 2007.
- [36] L. Xi, G. Liu, and J. Ni, "Autofocusing of ISAR images based on entropy minimization," *IEEE Trans. Aerosp. Electron. Syst.*, vol. 35, no. 4, pp. 1240–1252, Oct. 1999.
- [37] X. Mao, J. Wang, and X. Liu, "ISAR minimum-entropy phase adjustment based on gradient descent algorithm," *Modern Radar*, vol. 30, no. 1, pp. 40–43, 2008.
- [38] D. Huang *et al.*, "2D spatial–Variant phase errors compensation for ISAR imagery based on contrast maximisation," *Electron. Lett.*, vol. 52, no. 17, pp. 1480–1482, 2016.
- [39] J. Wang, L. Zhang, L. Du, D. Yang, and B. Chen, "Noise-robust motion compensation for aerial maneuvering target ISAR imaging by parametric minimum entropy optimization," *IEEE Trans. Geosci. Remote Sens.*, vol. 57, no. 7, pp. 4202–4217, Jul. 2019.
- [40] R. Eberhart and K. James, "Particle swarm optimization," in *Proc. IEEE Int. Conf. Neural Networks*, 1995, vol. 4, pp. 760–766.
- [41] Y. Shi and C. Russell, "Parameter selection in particle swarm optimization," in *Proc. Int. Conf. Evol. Program.*, 1998, pp. 591–600.
- [42] K. James, "Particle swarm optimization," *Encyclopedia of Machine Learning*, Berlin, Germany: Springer, 2010, pp. 760–766.
- [43] Z. Bao, M. Xing, T. Wang, *Radar imaging technology*. Beijing, China: Publishing House of Electronics Industry, 2005, pp. 24–40.
- [44] J. Mayhan, M. Burrows, K. Cuomo, and J. E. Piou, "High resolution 3D Snapshot ISAR imaging and feature extraction," *IEEE Trans. Aerosp. Electron. Syst.*, vol. 37, no. 2, pp. 630–642, Apr. 2001.
- [45] J. Nocedal and W. Stephen, *Numerical Optimization*, Berlin, Germany: Springer Science and Business Media, pp. 192–220, 2006.
- [46] F. Angel, A. Omar, and G. Jesus, "Facet model of moving targets for ISAR imaging and radar back-scattering simulation," *IEEE Trans. Aerosp. Electron. Syst.*, vol. 46, no. 3, pp. 1455–1467, Jul. 2010.
- [47] D. Ciunzo, G. Romano, and R. Solimene, "Performance analysis of time-reversal MUSIC," *IEEE Trans. Signal Process.*, vol. 63, no. 10, pp. 2650–2662, May 2015.
- [48] D. Ciunzo, "On time-reversal imaging by statistical testing," *IEEE Signal Process. Lett.*, vol. 24, no. 7, pp. 1024–1028, Jul. 2017.

**Yejian Zhou** was born in Zhejiang Province, China, in 1993. He received the B.S. degree in electronic engineering from Xidian University, Xi'an, China, in 2015, where he is currently pursuing the Ph.D. degree in signal processing with the National Laboratory of Radar Signal Processing, Xidian University. He is also studying as a visiting Ph.D. Student in Department of Urban Planning and Environment, KTH Royal Institute of Technology. His research interests include ISAR imaging and image interpretation.

**Lei Zhang** was born in Zhejiang Province, China, in 1984. He received the Ph.D degree in 2011, from Xidian University in 2012. He is currently working as an associate Professor with School of Electronics and Communication Engineering, Sun Yat-Sen University (Shenzhen campus). His research interests are radar imaging (SAR/ISAR) and motion compensation.

**Shaopeng Wei** was born in Jinan, Shandong Province, China. He received the B.S. degree in electronic engineering from Xidian University, Xi'an, China, in 2017. He is currently pursuing the Ph.D. degree in signal processing at the National laboratory of Radar Signal Processing, Xidian University. His research interests are radar signal processing and radar imaging.

**Yunhe Cao** was born in Anhui Province, China. He received the B.S., M.S., and Ph.D. degrees from Xidian University, Xi'an, China, in 2001, 2004, and 2006, respectively. He is currently working as a Professor in National Laboratory of Radar Signal Processing, Xidian University. His research interests include MIMO radar, digital array radar, adaptive signal processing, and target detection.